Supplement of The Cryosphere, 16, 2725–2743, 2022
https://doi.org/10.5194/tc-16-2725-2022-supplement
© Author(s) 2022. CC BY 4.0 License.

The Cryosphere Open Access EGU

Supplement of

A probabilistic framework for quantifying the role of anthropogenic climate change in marine-terminating glacier retreats

John Erich Christian et al.

Correspondence to: John Erich Christian (jchristian41@gatech.edu)

The copyright of individual parts of the supplement might differ from the article licence.

S1 Model equations and parameters

S1.1 Ice dynamics

We use a flowline model solving the 1-D Shallow-shelf approximation for ice flow. This assumes that flow is dominated by longitudinal stretching and basal sliding, and the stress balance is:

$$\rho_i g h \frac{\partial s}{\partial x} = \frac{\partial}{\partial x}\left(2hA^{-\frac{1}{n}}\left|\frac{\partial u}{\partial x}\right|^{\frac{1}{n}-1}\frac{\partial u}{\partial x}\right) - C|u|^{m-1}u. \quad (1)$$

This equation expresses how driving stress (left-hand side) is balanced by a combination of longitudinal stretching (right-hand, first term) and basal drag (right-hand, second term). ρ_i is the density of ice (917 kg m^{-3}), g is acceleration due to gravity (9.81 m s^{-2}), h is local ice thickness, and $\partial s/\partial x$ is the surface slope. u is the horizontal ice velocity, and A and n are the Glen flow coefficient and exponent, respectively ($A = 4.23 \times 10^{-25}$ Pa^{-3}s^{-1}; $n = 3$). C and m are the sliding coefficient and exponent, respectively ($C = 7 \times 10^6$ Pa m$^{-1/3}$s$^{1/3}$; $m = 1/3$), which here assume a Weertman-type sliding relationship.

The evolution of local ice thickness h is expressed by a continuity equation,

$$\frac{\partial h}{\partial t} = S - \frac{\partial (uh)}{\partial x}, \quad (2)$$

where S is the local surface mass balance.

The terminus is assumed to always be at flotation, and thus the thickness boundary condition there is

$$h_f = -\frac{\rho_w}{\rho_i} b(x_g), \quad (3)$$

where ρ_w is the density of seawater (1028 kg m^{-3}), and $b(x_g)$ is the (negative) bed elevation at the terminus position. We assume the terminus is not buttressed by an ice shelf, and so following Schoof (2007), the velocity boundary condition at the terminus is

$$2A^{-\frac{1}{n}}\left|\frac{\partial u}{\partial x}\right|^{\frac{1}{n}-1}\frac{\partial u}{\partial x} = \frac{1}{2}\rho_i g h\left(1 - \frac{\rho_i}{\rho_w}\right). \quad (4)$$

The inland boundary is assumed to be an ice divide where horizontal velocity is zero.

We follow the numerical implementation described in detail in Schoof (2007). The thickness (h) and velocity (u) equations are scaled to a grid from $\sigma = 0$ to $\sigma = 1$, where the grounding line always corresponds to the grid point at $\sigma = 1$. The grid thus stretches with grounding-line variations. The h and u grids are staggered such that the last u-grid point corresponds to the grounding line, and the last h-grid point where thickness is solved from the continuity equation is a half grid spacing (i.e., $\Delta\sigma/2$) upstream from the grounding line. However, the grounding line thickness h_f is also solved at $\sigma = 1$ via the flotation condition (Fig. 1).

The equations are solved using finite differences with an implicit time step. The continuity equation (Eq. 2) is discretized with an upwind scheme. Schoof (2007) provides a full description of the numerics. However, one difference from Schoof (2007) is that we have added frontal ablation at the terminus, described as follows and illustrated in Fig. 1. Generally, flux

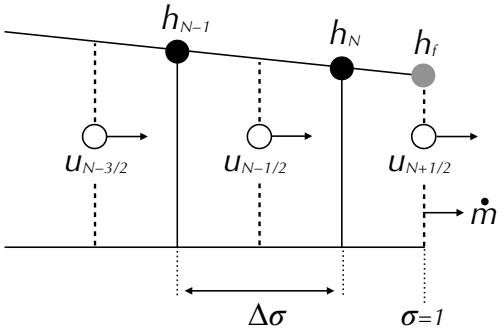

Figure S1. Schematic diagram for numerical grid near the grounding line. Velocities are solved at grid points marked by open circles. Thickness is solved via the continuity equation at grid points marked by black circles, and via the flotation condition at the gray point. The continuity equation thus requires interpolating u to the h grid to calculate flux divergence. For the point h_N, this also includes a flux term from frontal ablation ($\dot{m}$).

divergence at a thickness gridpoint i is discretized as

$$\frac{\partial}{\partial x}(hu) \sim \frac{h_i(u_{i-1/2} + u_{i+1/2}) - h_{i-1}(u_{i-3/2} + u_{i-1/2})}{2\Delta\sigma}. \tag{5}$$

Note that u must be interpolated because of the staggered grid, both at the thickness point i and its "upwind" point $i-1$. At the last thickness grid point ($i = N$), there is an extra term in the output flux to account for the frontal ablation rate $\dot{m}$:

$$\frac{\partial}{\partial x}(hu) \sim \frac{h_N\big(u_{N-1/2} + u_{N+1/2} + \dot{m}\frac{h_f}{h_N}\big) - h_{N-1}\big(u_{N-3/2} + u_{N-1/2}\big)}{2\Delta\sigma}. \tag{6}$$

Note that because it is assumed to occur at $N + 1/2$ where the thickness is h_f (Fig. 1), it must be scaled by $\frac{h_f}{h_N}$. This frontal ablation is a very general flux anomaly at the terminus. Its effect is to require additional input flux to the the last grid point to balance the continuity equation. Because the terminus is constrained to be at flotation, this results in a steeper surface slope just upstream of the terminus.

S1.2 Generating synthetic climate variability

We assume that an order-one autoregressive process (AR-1) approximates the variability in surface mass balance and frontal ablation on annual and longer timescales. This is a common and parsimonious model for climate variability with persistence (e.g., Hasselmann, 1976). To generate random anomalies, we use a method following Percival et al. (see also Roe and Baker, 2016; Christian et al., 2020). The desired temporal properties (i.e., the persistence timescale of the variability) are specified in the power spectrum. For a discrete AR-1 process, the power as a function of frequency f is

$$P(f) = P_0\big(1 + r^2 - 2r\cos(2\pi\Delta t f)\big)^{-1}, \tag{7}$$

where P_0 scales the total variance and r is the auto-correlation at a lag of Δt (here, 1 yr). The persistence timescale is related to r by $\tau_{AR1} = \frac{\Delta t}{1-r}$. The power can thus be defined at the discrete Fourier frequency components, which are set by the length

and sampling interval of the desired timeseries. To get a complex spectrum (i.e., with both power and phase information), each discrete frequency component is then multiplied by a random phase rotation e^{ϕ} where ϕ is uniformly distributed between 0 and $2\pi i$. The inverse Fourier transform of this complex spectrum then yields a timeseries of AR-1 variability. Finally, we scale the magnitude of the variability as needed. By using the same set of random phases but different τ_{AR1}, it is possible to generate multiple timeseries that have different spectral characteristics but some correlation in the time domain. This is advantageous for analyzing the effects of persistence in isolation, or for emulating some partial correlation in different climate variables.

S2 Convergence Tests

We conducted convergence tests to understand how the choice of grid size and time steps may affect our results. A notable consequence of our frontal ablation scheme is that although it is conceptually a horizontal flux (Fig. S1), it is numerically equivalent to a surface ablation term at the last grid point. However, since the flux is scaled by thickness ($\dot{m}\ h_f$) rather than the grid spacing, as for surface mass balance ($S\Delta x$) , its "drawdown" tendency on the last thickness point depends on the grid spacing. There is a local steepening effect that increases for smaller Δx, and would lead to a singularity for arbitrarily small Δx (see Supplementary material of Bassis et al., 2017). We tested a range of grid sizes from approximately 30 to 190 m, and found that this does affect the steady state profile and terminus position (Fig. S2a,b). For grid spacing below 30 m, the model failed to converge. This has little effect on the dynamics of glacier fluctuations except for a small offset (Fig. S2c); however, this can be the difference between sustained retreat vs. recovery in edge cases (Fig. S2d), so could be expected to have a similar affect on the probability of retreat as other parameter perturbations. We used consistent gridding schemes whenever comparing different ensembles, so we expect this has little effect on our conclusions. However, it is one model choice (among many) to be aware of which may bear on simulations of noise-driven retreat.

In most of our simulations, we used a model time step of 5 years, in which case we averaged the annually-sampled stochastic forcing over the time step. This has little effect on the character of fluctuations compared to a 1-year time step (Fig. S3).

S3 Estimating probabilities from ensemble simulations

S3.1 Dependence on spinup interval

As described in the main text, a stochastic spinup period is needed prior to estimating the probability of retreat, as we aim to draw from a range of initial conditions consistent with natural climate variability. The spin period must be adequately long partly to fill out this distribution, and also to avoid the effects of noise-induced drift that occurs when stochastic forcing is first initiated. We can illustrate this drift via the ensemble-mean terminus position for simulations with few or no unstable retreat (Fig. S4). This also illustrates how the initial steady-state position biases the probability of retreat (Fig. S4b), underscoring the need for an adequately long spinup.

Even beyond noise-induced drift, it is important to understand whether the probability of retreat, as estimated from the ensembles, is constant in time. We are estimating the probability as n_r/n_s, where n_r is the number of retreats in an experimen-

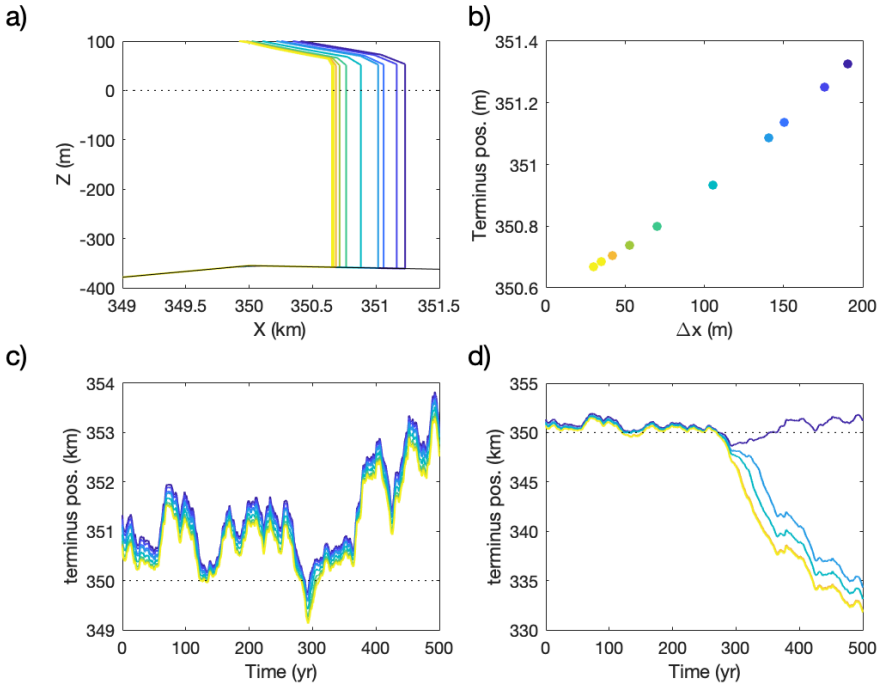

Figure S2. Convergence test for grid size. (a) shows steady state profiles near the terminus. (b) plots steady-state terminus against grid size. (c) shows terminus fluctuations for each grid size, forced by random frontal ablation. (d) shows fluctuations with a trend added, which causes retreat for some cases. For the simulation with the coarsest grid size, the offset in terminus position (i.e., (a) and (b)) is enough to prevent retreat in this particular case. This indicates that under this frontal ablation scheme, the probability of retreat could be sensitive to grid size due to its effect on steady-state position, in the same way other parameter perturbations affect the probability of retreat (i.e., Fig. 3 in the main text).

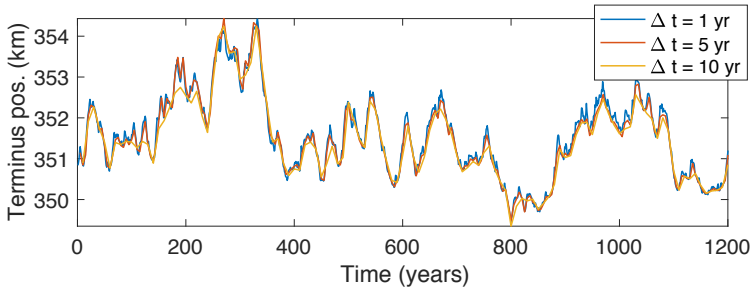

Figure S3. Convergence test for the model time step, from $\Delta t = 1$–10 years. Fluctuations driven by frontal ablation variability are damped slightly for longer timesteps, as yearly climate anomalies are averaged over the time step. However, since high freqencies are already strongly damped by ice dynamics, the effect on overall glacier variability is minimal. We use model timesteps of 1–5 years throughout our experiments.

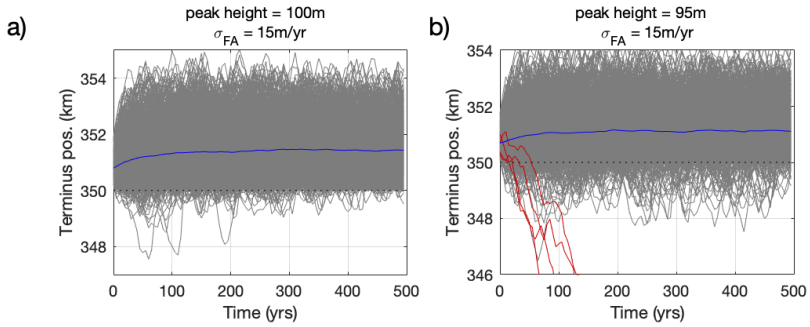

Figure S4. (a) Noise-induced drift can be illustrated via the ensemble-mean terminus position (blue line) in cases with no unstable retreats (which would bias the mean). The drift decays over roughly century timeframes. (b) as for (a), but with a slightly lower bed peak, which moves the system closer to the threshold. Note that a few retreats occur initially, but none after the noise-induced drift decays. This illustrates how the probability of retreat is inflated shortly after starting from the steady-state initial condition, which is closer to the peak than the long-term mean. The same effect occurs for cases with non-zero long-term probabilities of retreat.

tal interval ($t_1 < t < t_2$), and n_s is the number of ensemble members that have survived the initialization period ($0 < t < t_1$) without retreating. Note that n_s diminishes as more and more glaciers retreat. This fraction n_r/n_s is fundamentally a conditional probability—i.e., the probability of retreat in the experimental interval, conditioned on the fact that a glacier hasn't yet retreated. This conditional probability is most relevant for the attribution question focused on some particular observed retreat. However, it is worth comparing to the joint probability n_r/N, where N is the total ensemble size (i.e., the probability of any of the N ensemble members surviving the experimental interval, *and* then retreating during the observational interval).

We calculate both n_r/n_s and n_r/N over progressive 100-year intervals of two 2000-year, 5000-member ensemble runs (Fig.S5). The probability of retreat is enhanced in the first couple of centuries, before the noise-induced drift stabilizes. n_r/n_s is fairly stable, but with some caveats. There is some jitter due to sampling error (discussed below), as well as a long-term increase over 2000 years. We infer that the latter is because the variance of glacier fluctuations is under-sampled initially, due to the millennial timescales of interior ice dynamics (Robel et al., 2018), which are sensitive even to forcing at the terminus (Christian et al., 2020). The ratio n_r/n_s also becomes less stable as the ensemble size decreases. Note that n_r/N continually decreases; the rate of retreats drops off with the number of surviving ensemble members.

Note that this behavior roughly approximates a Poisson process, where the probability of an event occurring in some fixed interval would be constant. Of course, each glacier can only retreat once, but across the ensemble, the (conditional) probability of retreats per unit time would be constant for a pure Poisson process. There are some caveats due to the timescales of memory, but it this can still be a useful statistical model to keep in mind.

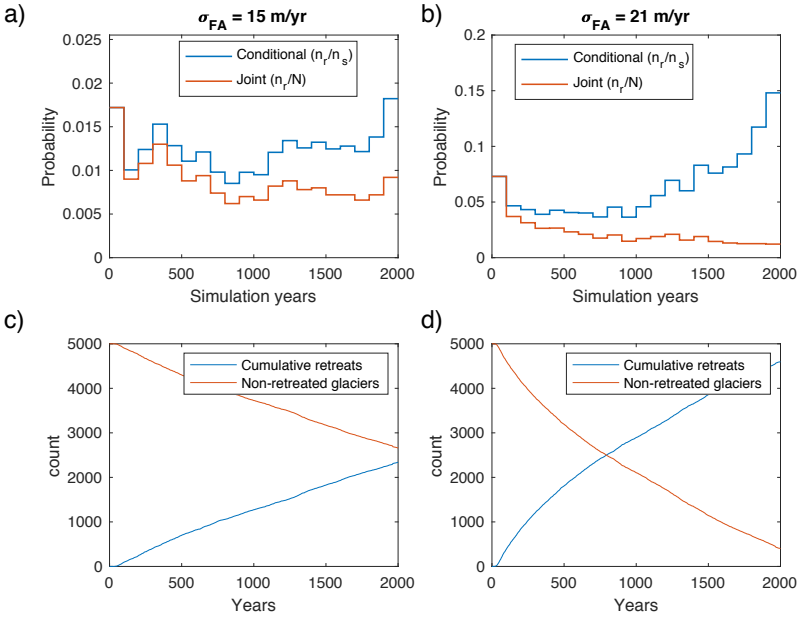

Figure S5. (a) Probabilities of retreat over 100-year intervals in a 2000-year, 5000-member ensemble run, with a bed peak height of 94 m and $\sigma_{FA} = 15$ m/yr. Blue markers track the conditional probability (the metric used in our analyses). Red markers track the joint probability, which decays as more and more ensemble members retreat. Note the effects of the initial condition in the first century or two, and the long-term rise in conditional probability (b) As for (a), except with $\sigma_{FA} = 21$ m/yr. (c) Cumulative retreats (blue) and non-retreated glaciers (red) throughout the 2000-year ensemble simulation with $\sigma_{FA} = 15$ m/yr. (d) As for (c), except with $\sigma_{FA} = 21$ m/yr.

S3.2 Sampling error for estimated probability

Estimating the probability of retreat based on the number of retreats within a finite ensemble introduces the possibility of sampling error. We stress that this would be only one source of error in an attribution assessment for any particular glacier. However, it is useful to understand how this error varies with ensemble size. In our simulations, the probability of retreat within a particular time interval ($t_1 < t < t_2$) depends on the choice of time interval, model parameters, and definition of a retreat event – in short, all of the choices defining the model simulation. For a fixed set of such choices, however, each independent simulation can be considered a Bernoulli trial with probability p of producing retreat within the chosen interval. The aleatory ensemble is a sequence of Bernoulli trials from which we estimate p as $\hat{p} = n_r/N$ (often termed the binomial proportion), where again n_r is the number of simulations producing retreat between t_1 and t_2 (i.e., "successesful" Bernoulli trials) and N the ensemble size (i.e., number of trials). Note that p as described this way corresponds to the joint probability of no retreats before t_1 and one retreat between t_1 and t_2; let this be $\hat{p_1}$. The independent probability of no retreat before t_1 can also be put in terms of Bernoulli trials and estimated from the ensemble (n_s/N); let his be $\hat{p_2}$.

For large samples of Bernoulli trials where errors in $\hat{p}$ are approximately normally distributed, a common approximation for the standard error S is

$$S = \sqrt{\frac{\hat{p}(1-\hat{p})}{N}}. \tag{8}$$

Ultimately, however, we are interested in the conditional probability $\hat{p_3} = \hat{p_1}/\hat{p_2} = n_r/n_s$. If we make the simplifying assumption that $\hat{p_1}$ and $\hat{p_2}$ are independent, we can combine them to estimate the standard error of $\hat{p_3}$ using the variance formula:

$$S_3 = \sqrt{\left(\frac{\partial \hat{p_3}}{\partial \hat{p_1}}\right)^2 S_1^2 + \left(\frac{\partial \hat{p_3}}{\partial \hat{p_2}}\right)^2 S_2^2} = \sqrt{\left(\frac{1}{\hat{p_2}}\right)^2 S_1^2 + \left(\frac{\hat{p_1}}{\hat{p_2}^2}\right)^2 S_2^2}. \tag{9}$$

It should be noted this is a fairly rough approximation, as the normal approximation breaks down for $\hat{p}$ very close to 1 or 0. Additionally, $\hat{p_1}$ and $\hat{p_2}$ are not strictly independent (one less retreat prior to t_1 is one more chance to retreat between t_1 and t_2, though is a small effect if that chance ($\hat{p_1}$) is low; or if N is large). However, we also conducted Monte-Carlo trials of a simpler threshold-crossing process with a similar range of probabilities (not shown), and found Eq. 9 to be a good approximation to empirical estimates of the conditional probability.

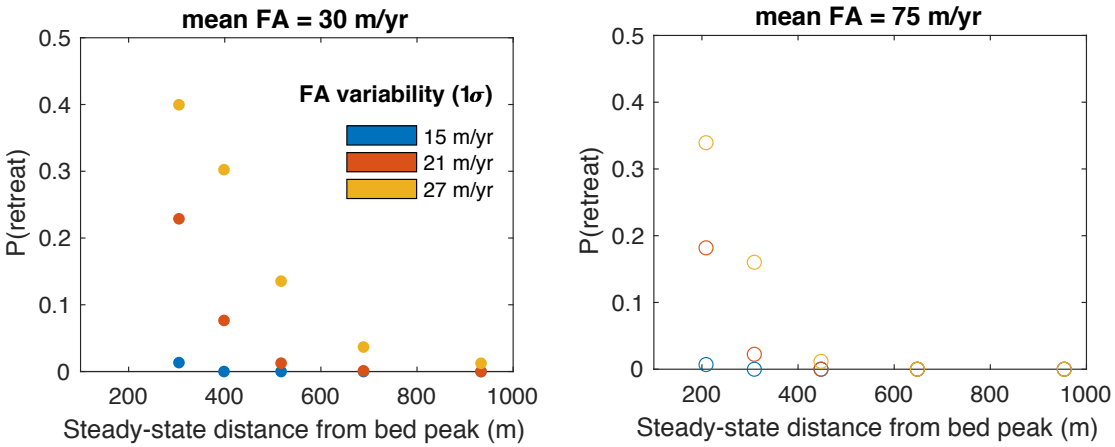

Figure S6. Ensemble retreat probabilities across variations in bed-peak height (which affect the steady-state distance from the bed peak) and the amount of frontal ablation variability. a) Results for the original idealized glacier, which has mean frontal ablation of 30 m/yr, meaning that the lower bound of zero frontal ablation truncates some anomalies, especially for greater σ_{FA}. b) as for a), except for a glacier with mean frontal ablation of 75 m/yr, which minimizes the effect of the zero bound. In either case, however, increasing σ_{FA} can have a large effect on the probability of retreat.

S4 Effect of different frontal ablation assumptions

Throughout our experiments, we impose frontal ablation anomalies drawn from distributions with $\sigma_{FA} = 12$–27 m/yr, but in the numerical model we stipulate a lower bound of zero absolute frontal ablation. This avoids numerical issues associated with adding ice at the terminus. However, it means that the most extreme negative anomalies are truncated, and the variability is more asymmetric for greater σ_{FA}. Compared to a symmetric distribution of frontal ablation anomalies, this increases the time-mean of frontal ablation, and therefore moves the time-mean of the terminus fluctuations inland (i.e., closer to the bed peak in our idealized geometry). In principle, this affects the probability of retreat from the bed peak. Thus, our analysis in Fig. 3 of the main text does not fully separate the two effects of proximity to the bed peak and magnitude of variability upon the probability of retreat, because increasing the magnitude of σ_{FA} also pushes the glacier closer to the bed peak, on average.

To assess this effect, we also considered a glacier with a higher mean frontal ablation (75 m/yr), so that the zero-bound plays little role for the same range of σ_{FA}. That is, for the strongest variability of $\sigma_{FA} = 27$ m/yr, the lower bound on variability is approximately 2.8σ. To compensate for higher frontal ablation while still yielding a similar steady-state terminus position, we uniformly raised the entire bed with respect to sea level (approximately 60 m), bed kept the dimensions of the bed peak the same with respect to the surrounding topography.

We compare the retreat probabilities in perturbed parameter ensembles for these two glaciers, adjusting the bed-peak height to change the steady-state terminus position (Fig. S2). Panel (a) shows results from the original glacier (i.e., a subset of results from Fig. 3c of the main text), while panel (b) shows results for the glacier with higher mean frontal ablation. Note that the

steady-state distances from the bed peak (and the relation between bed-peak *perturbations* and this distance) are not exactly the same between glaciers. However, the general results are the same: proximity to the bed peak and the magnitude of climate variability are clear controls on the probability of retreat. Thus, while a zero-bound on frontal ablation may contribute slightly to the increased probability of retreat as σ_{FA} is increased, it appears the main effect of larger σ_{FA} is simply the addition of larger climate perturbations. As shown above (Fig. S4), other nonlinearities also affect the mean terminus position as variability is introduced or increased. These issues have to be considered when initializing any simulation with noisy forcing, and motivate the transient spinup period in our simulations.

S5 Synthetic attribution experiments for a range of parameters

Here we provide additional synthetic attribution analyses with different parameter choices. This helps illustrate the range of probabilities that might be encountered in ensemble experiments, as well as the amounts by which an anthropogenic forcing trend changes the probability of retreat. Frontal ablation trends are applied over the full 150-year experimental interval, and except where noted, the glacier geometry and parameters are as described in the main text.

First, we consider consider a glacier with a higher bed peak (94 m) in order to lower the null probability of rapid retreat (the simulations in Fig. 5 of the main text assumed a bed peak of 90 m) . We apply the same σ_{FA} and Δ_{FA} as in the main text (18 m/yr and 24 m/yr, respectively), with Δ_{FA} applied over the entire 150-year simulation. The trend increases the probability of retreat to approximately 0.5 (Fig. S3a). Such a case would constitute a strong probabilistic attribution statement, since rapid retreat is very unlikely ($P < 1\%$) in the absence of a trend, and thus the multiplier on probability is large. However, that only 50% of simulations produce rapid retreat even with the trend indicates that retreat is still partially contingent on internal variability.

As an alternative case, we consider stronger natural variability ($\sigma_{FA} = 24$ m/yr) and 90 m bed peak, which increase the null probability of retreat to approximately 0.25 (Fig. S3b). A trend of $\Delta_{FA} = 32$ m/yr (giving the same ratio of Δ_{FA}/σ_{FA}) increases the retreat probability to 0.81. This is still a marked increase—more than tripling the likelihood of rapid retreat—but is distinct from a case where rapid retreat is nearly impossible without a trend.

Finally, to generalize further, we aggregate results from multiple ensembles in Fig. S4. Probability of retreat is plotted against the magnitude of the forcing trend, with colors denoting different assumptions about the magnitude of variability and the time of onset of the trend. In all cases, the probability of retreat tends towards unity as Δ_{FA} increases. However, differences in σ_{FA} (blue, red, and yellow markers) affect how rapidly the probability increases (and its baseline in the absence of a trend). Additionally, a trend concentrated in the last 50 years (purple markers) is again seen to increase the probability of retreat less than the early-onset trends.

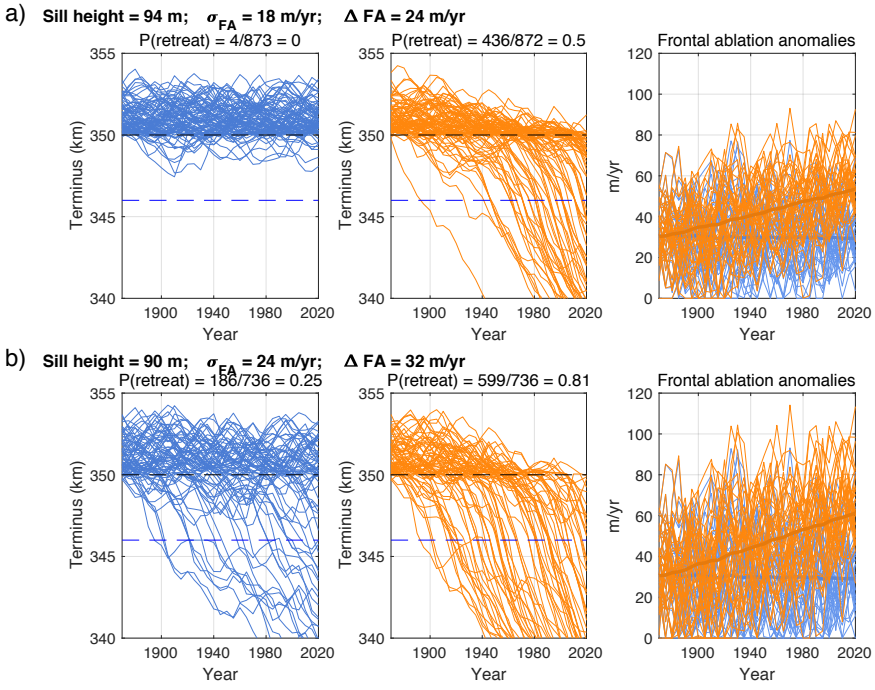

Figure S7. Synthetic attribution experiments with different parameter choices (compare to Fig. 5 in the main text). For clarity, not all simulations are plotted. Left panels show simulations with no trend, center panels show simulations with an anthropogenic trend, and right panels show the frontal ablation anomalies for both scenarios. a) Simulations assuming a slightly higher bed peak, yielding a lower null probability of rapid retreat, and significantly increased probability due to the frontal ablation trend. b) Simulations assuming stronger stochastic frontal ablation variability, yielding higher null retreat probability. A frontal ablation trend still increases the probability of retreat, though by a lesser fractional amount.

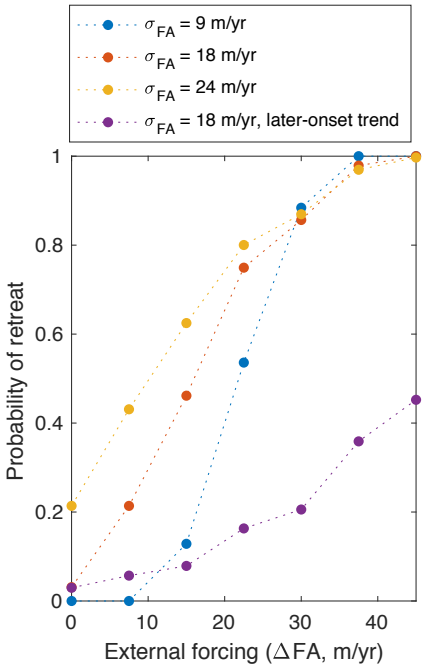

Figure S8. Retreat probabilities from 28 ensemble simulations with different frontal ablation variability and trends. Results are plotted against the total frontal ablation trend, with colors corresponding to differences in the variability or trend onset as indicated. Purple markers correspond to trends applied only over the last 50 years of the 150-year experimental interval; all others assume a 150-year trend.

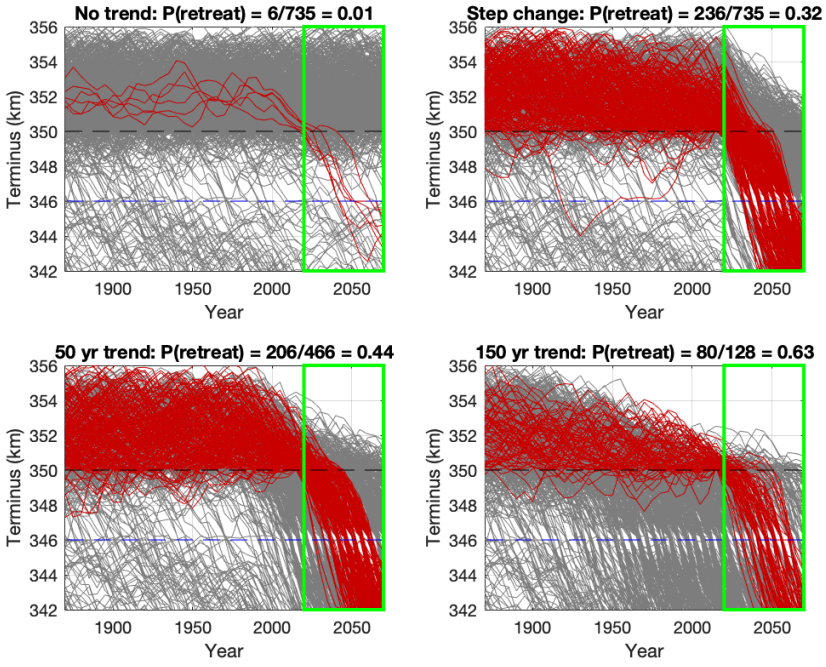

Figure S9. Here we focus on the 50 years after four different forcing scenarios: No trend (a); a step change at 2020 (b); a 50 year trend from 1970–2020 (c); and a 150-year trend from 1870–2020 (d). The total changes in frontal ablation are the same, so that after 2020 the distribution of frontal ablation is the same in each scenario (with the exception of (a)). Differences in the probability of retreat from 2020–2070 (green boxes) therefore show the effects of past forcing, namely that long-term trends push the average terminus position closer to the bed peak. Note that the effective ensemble size drops off under long term trends because many retreats occur during the trend, but the overall effect of the trend is clear.

S6 Isolating the effect of lagged ice dynamics

As noted in the main text, an external climate trend has two distinct effects on the probability of retreat: first, it makes any short-term frontal ablation anomaly more positive. Additionally, it gradually drives the glacier closer to the bed peak than it otherwise would be. The evolution of the latter effect depends on the response timescales of ice dynamics, or in other words, how long these dynamics have been integrating the climate anomaly. Figure S9 shows the conditional probability of retreat in the 50 years *after* different forcing scenarios. This is a way to isolate the lagged effect of ice dynamics, and shows this effect plays a large role in the increased probability of retreat under century-scale trends.

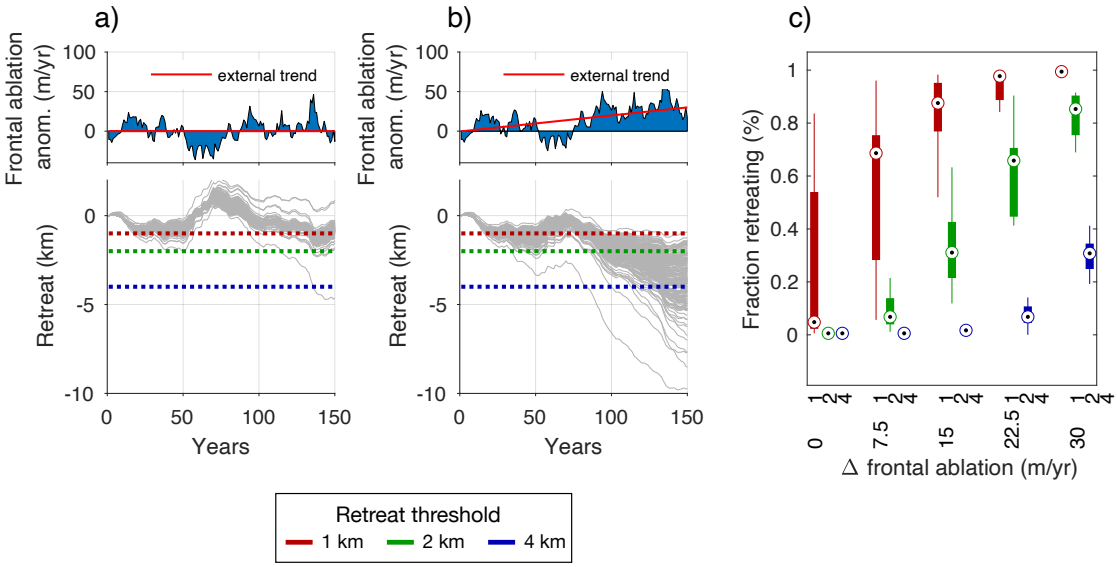

Figure S10. Simulations for the population of glaciers (compare to Fig. 7 of main text). (a) Terminus change (relative to year 0) for each glacier, all forced with the same frontal ablation anomalies (top), which have no external forcing trend. Dashed lines show retreat thresholds. (b) as for (a), except with an external forcing trend in frontal ablation, with a total increase of 30 m/yr over 150 years. (c) Box plot showing proportion of glaciers in the population exceeding the retreat threshold, across six trend scenarios. "Δ frontal ablation" refers to the total linear trend over 150 years. For each level of forcing trend, 20 simulations of the glacier population are run with different realizations of climate variability, with the distribution of retreats indicated with box-and-whisker markers for each retreat threshold.

20

S7 Alternative retreat metrics for population of glaciers

In Fig. S10, we show the same synthetic attribution experiment for the population of glaciers as in the main text (Fig. 7), but with multiple retreat thresholds (1, 2, and 4 km). Because each glacier has a different proximity to the closest bed peak (see Fig. 6c), a single retreat threshold applied to the population is somewhat arbitrary. The fraction of glaciers counted as retreating depends on the threshold for retreat, but considering multiple thresholds shows that fraction increases with higher forcing trends regardless of threshold (Fig.S10c).

S8 Advance on bumpy topography

In Fig. S11, we show the response of 50 glaciers on random bumpy topography (i.e., a subset of the population described in the main text) following an increase in surface mass balance (along with stationary variability in frontal ablation). Glaciers advance to varying degrees, with some exhibiting large, rapid advances when they encounter retrograde bed slopes. This demonstrates the advancing case of the basic marine-ice-sheet instability mechanism (e.g., Schoof, 2007). In such a case, it is glaciers closest

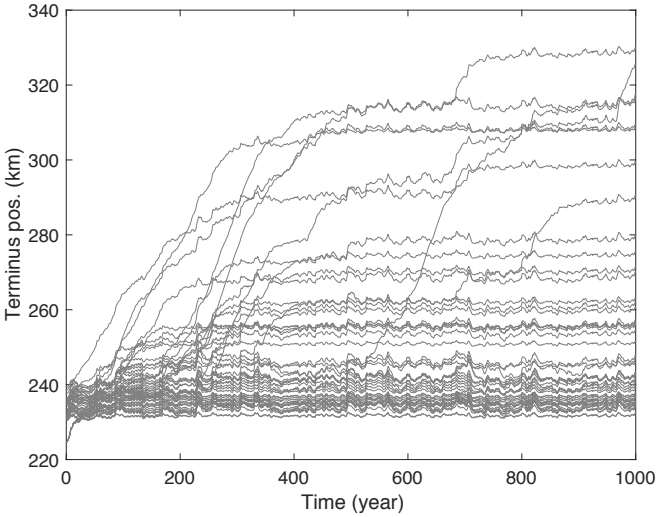

Figure S11. Response of 50 glaciers to a 30% increase in surface mass balance (along with stationary variability in frontal ablation). Each glacier has unique and random bed topographies, as described in the main text. Termini advance through the bumpy topography, including some cases with large rapid advances when they encounter retrograde slopes.

to retrograde slopes in the *seaward* direction that exhibit unstable advances. That is, glacier configurations with a relatively high probability of rapid retreat are likely to be different than those with a relatively high probability of advance.

Code availability. Code for the core glacier model is available as a persistent Zenodo repository at https://doi.org/10.5281/zenodo.5245271 (Robel, 2021). Additional code for the ensemble analysis within this study, as well as model output and scripts to recreate figures, is also available as a persistent Zenodo repository at https://doi.org/10.5281/zenodo.6525750 (Christian, 2022).

References

Bassis, J. N., Petersen, S. V., and Mac Cathles, L.: Heinrich events triggered by ocean forcing and modulated by isostatic adjustment, Nature, 542, 332–334, https://doi.org/10.1038/nature21069, 2017.

Christian, J. E.: Marine-terminating-glacier stochastic retreat (release of code for publication), https://doi.org/10.5281/zenodo.6525750, 2022.

Christian, J. E., Robel, A. A., Proistosescu, C., Roe, G., Koutnik, M., and Christianson, K.: The contrasting response of outlet glaciers to interior and ocean forcing, The Cryosphere, 14, 2515–2535, https://doi.org/10.5194/tc-14-2515-2020, 2020.

Hasselmann, K.: Stochastic climate models Part I. Theory, Tellus, 28, 473–485, https://doi.org/10.3402/tellusa.v28i6.11316, 1976.

Percival, D. B., Overland, J. E., and Mofjeld, H. O.: Interpretation of North Pacific Variability as a Short-and Long-Memory Process, Journal of Climate, 14, 4545–4559, https://doi.org/10.1175/1520-0442(2001)014<4545:IONPVA>2.0.CO;2.

Robel, A. A.: aarobel/SSAsimpleM: Release of SSAsimpleM for publication, https://doi.org/10.5281/zenodo.5245271, 2021.

Robel, A. A., Roe, G. H., and Haseloff, M.: Response of Marine-Terminating Glaciers to Forcing: Time Scales, Sensitivities, Instabilities, and Stochastic Dynamics, Journal of Geophysical Research: Earth Surface, 123, 2205–2227, https://doi.org/10.1029/2018JF004709, 2018.

Roe, G. H. and Baker, M. B.: The response of glaciers to climatic persistence, Journal of Glaciology, 62, 440–450, https://doi.org/10.1017/jog.2016.4, 2016.

Schoof, C.: Ice sheet grounding line dynamics: Steady states, stability, and hysteresis, Journal of Geophysical Research: Earth Surface, 112, https://doi.org/10.1029/2006JF000664, 2007.